Published in final edited form as:
J Magn Reson. 2007 May ; 186(1): 105–111. doi:10.1016/j.jmr.2007.01.021.

Object dependent sweep width reduction with spectral-spatial EPR imaging

Kang-Hyun Ahn[1,2] and **Howard J. Halpern**[1,2,*]

[1] Department of Radiation and Cellular Oncology, University of Chicago, Chicago, Illinois

[2] Center for EPR Imaging in Vivo Physiology, University of Chicago, Chicago, Illinois

Abstract

For spectral-spatial EPR imaging, prior knowledge about the spatial support of an imaged object can be exploited in two ways. We can shrink the spatial field of view (FOV) to closely wrap the object in a sphere or reduce the sweep width in a projection dependent fashion. Use of a smaller spatial FOV with the same number of samples enhances spatial resolution by reducing voxel volume at the expense of signal-to-noise and a consequent degraded line width resolution. We have developed another approach to define sweep width that prunes away the portions of the projection sweep with no signal. This reduces data acquisition time for the continuous wave (CW) EPR image proportional to the sweep width reduction. This method also avoids voxel volume reduction. Using the reduced-sweep method, we decreased the data acquisition time by 20% maintaining spatial and linewidth resolution.

Keywords

EPR; 4D EPRI; Tomography; Spectral-spatial imaging; Region of interest sampling

Introduction

Electron paramagnetic resonance imaging (EPR imaging, EPRI) is capable of measuring the spatial and spectral distribution of the absorption. Useful information concerning local fluid environment is reported in the EPR spectra. One can design a variety of spin probes to be sensitive to specific aspects of physiology including temperature, pH, microviscosity, tissue oxygenation, and a distribution of exogenous paramagnetic species [1–6]. For an application of EPRI to *in vivo* physiology it is important to complete data acquisition in minimum time.

A spectral-spatial image is reconstructed from EPR projections obtained with stepped field gradients [7,8]. The extremely short spin-relaxation time of unpaired electrons makes the continuous wave (CW) EPRI technique common and technically less challenging for the EPR image acquisition, particularly at low operating frequencies. Unlike Fourier transform acquisition [9] or electron spin echo acquisition [10], the acquisition time of a CW EPRI is directly related to the spectral interval of its projections. If a more compact interval that retains

*Correspondence: Howard J. Halpern, Department of Radiation and Cellular Oncology, MC1105, University of Chicago Medical Center, 5841 S. Maryland Ave. Chicago, IL 60637, E-mail address: h-halpern@uchicago.edu, Telephone: +1-773-702-6871, Fax: +1-773-702-5940.

full information for the reconstruction can be determined from an imaged object, one can reduce data acquisition time of EPRI by employing the minimum magnetic field sweep intervals for projections.

Previous spectral-spatial CW EPR imaging evaluated projection spectral intervals using the concept that the support of the spectral-spatial object would lie entirely within the hypercylinder contained in the circumscribed hypersphere [11]. We have earlier discussed a simpler method of reduction of the sweep interval to the hypercylinder itself [12]. In that treatment, which assumed that the spectral dimension was covered with sinograms stepped in equal angles, the spatial dimension was reduced to the minimum spatial support of the object. For full coverage, this often requires the use of high gradients that either reduces the signal-to-noise of the projection below a useful value or requires gradient magnitudes that are unavailable. In this work, we attempt to avoid the limitations of the latter method by using a spectral-spatial 4D EPRI with sweep width reduced based on the object size.

The performance of EPRI was characterized in two ways. The spectral dimension from each voxel of the image of a homogeneous phantom was fit to an accurate parametric spectral shape [13,14], producing a 3D EPR line-width map. One criterion used to judge the quality of a set of images was the scatter of the spectral line-width distribution from a homogeneous sample. This increases as the signal-to-noise ratio (SNR) goes down. The other figure of merit was the spatial resolution of a 3D EPR signal height map. We observed a trade-off relationship between the spatial resolution and the line-width resolution when the spatial field of view (FOV) was varied instead of the sweep width.

Background and Theory

Projections of the spectral-spatial EPRI are taken with gradients of various directions and magnitudes. The variation of the gradient magnitude G is characterized by a spectral angle α defined as [11]

$$\tan\alpha = G\Delta L/\Delta B, \tag{1}$$

where ΔL is a spatial FOV that must be fully sampled, and ΔB is a magnetic field interval, or spectral FOV that fully encloses the EPR signal obtained without gradient. Sampled volume of the spectral-spatial image is a hyper-cylinder, which collapses to a square (shade in Fig 1a) for a 2D spectral-spatial image. For a spectral-spatial object with finite support (ΔB, ΔL), one wishes to sample the spectral axis of [$-\Delta B/2$, $\Delta B/2$] at every spatial position in ΔL.

For a 4D spectral-spatial object, the projections can be interpreted as 4D Radon transforms of the 1D spectral and 3D spatial object function. A generalized four-dimensional space is defined with a unified unit by introducing a conversion factor $c=\Delta B/\Delta L$, and a 4D unit vector $\widehat{\alpha}_G=(\cos\alpha, \sin\alpha\vec{G}/G)$ associated with a magnetic field gradient $\vec{G}$. EPR signal $s(B_{SW}, \vec{G})$ measured at a particular B_{SW} under the gradient $\vec{G}$ is written as is discussed more fully in [12]

$$\begin{aligned} s(B_{sw}, \vec{G}) &= \iint f(B, \vec{x})\delta(B-(B_{sw}-\vec{G}\cdot\vec{x}))d\vec{x}\,dB \\ &= \cos\alpha \int f(\vec{r})\delta(\xi-\widehat{\alpha}_G\cdot\vec{r})d\vec{r}, \\ \vec{r} &= (B, c\vec{x}), \\ \xi &= \cos\alpha B_{sw}, \end{aligned} \tag{2}$$

where $f(B, \vec{x})$ is a four-dimensional spectral-spatial resonance density that denotes energy absorption at a spatial location $\vec{x}$ for an external magnetic field B.

A conventional filtered backprojection (FBP) algorithm requires a full sampling in a sphere that encompasses the hyper-cylinder, with the corresponding sweep width of [11]

$$\Delta B_{\mathrm{sw}} = \frac{\sqrt{2}\Delta B}{\cos\alpha}. \tag{3}$$

Williams *et al.* [12] define a minimum sweep width that covers the hyper-cylindrical sampled volume as

$$\Delta B_{\mathrm{sw}} = \Delta B(1+\tan\alpha). \tag{4}$$

The above definitions of sweep width of Eq. (3) and Eq. (4) are diagrammed in Fig. 1a and 1b. We define $\Delta B_{\mathrm{SW}} = \Delta\xi/\cos\alpha$ and $c\Delta L = \Delta B$ in Fig. 1b.

The spatial extent of the spectral spatial object is determined by two factors. One is the physical size of the object in which spin probes are distributed, and the other is the distribution of the RF field. If either of the two is enclosed by ΔL, we have full support for the object that produces EPR signal. The segments of a circle outside the shaded area in Fig. 1a are devoid of signal.

Suppose we have a spatial extent of object $\Delta L'$, which we call the region of interest or ROI, that is known to be smaller than the arbitrarily chosen spatial FOV ΔL. We can assign $\Delta L'$ to the spatial FOV (Fig. 1c) with a redefinition of the conversion factor $c' = \Delta B/\Delta L'$. This results in a zoomed-in image with the spectral angle α defined as

$$\tan\alpha = G\Delta L'/\Delta B, \tag{5}$$

which requires higher magnitude of gradient compared with the same spectral angle of Eq. (1). The spatial FOV can be chosen, for example, to limit the maximum gradient to that which can be safely generated by the gradient coils. Fig. 2c shows a signal height slice of the EPR image obtained with the spatial FOV zoomed in by 20% compared to the EPR image of Fig. 2b.

Instead of the zoomed-in sweep, we can define an ROI, $\Delta L'$ and modify the spectral-spatial imaging to exploit this information. Fig. 2a and 2b shows a phantom and its EPR image with the spatial FOV of diameter ΔL. The sweep width and gradient defined by Eq. (1) and Eq. (3) will provide projections for the conventional spectral-spatial imaging. Fig. 1d describes the reduction of sweep width when the spatial FOV is larger than the ROI. This leads to the following definition of sweep width as

$$\begin{aligned} \Delta B_{\mathrm{sw}} &= \Delta\xi/\cos\alpha \\ &= (\Delta B\cos\alpha + c\Delta L'\sin\alpha)/\cos\alpha, \\ &= \Delta B(1+k\tan\alpha) \end{aligned} \tag{6}$$

where $k = \Delta L'/\Delta L$, and $\Delta B = c\Delta L$. This value of ΔB_{SW} is clearly smaller than the previous definition. By zero-padding at both ends of each acquired projection, we can obtain full-length

projection of Eq. (3) for the reconstruction. With the same set of gradients as in Eq. (1), the reduced sweep width of Eq. (6) decreases the data acquisition time.

Methods

Phantom construction and data acquisition

We used a phantom made of sealed borosilicate glass cylinder with 9.5 mm inner diameter and 45 mm length. The bottle was filled with 1 mM the deoxygenated trityl OX063 radical (methyl-tris[8-carboxy-2,2,6,6-tetrakis[(2-hydroxyethyl]benzo[1,2-d:4,5-d']bis [1,3]dithiol-4-yl]-, trisodium salt, MW 1427), a kind gift from Nycomed Innovations, Malmo SW.

The EPR images were taken using a spectroscopic imager operating at 250 MHz [15]. A single loop-single gap resonator (with a sample holding loop 16 mm in diameter and 15 mm in length) was used with a circulator based bridge with quadrature RF detection. The sensitive region of the resonator was 1.5 cm in diameter and approximately 2.5 cm along the axis of the resonator. We used an accurate lineshape simulation [13,14] to allow operation with over-modulation (17 μT modulation amplitude) to increase SNR. Field modulation was produced by a 7.5 cm radius Helmholtz coil pair operating at 4.98 kHz. The RF power delivered to the resonator was 0.020 mW, which was 10 times lower than the saturation level. Fourteen spectral projections were employed for 100 directions at uniform solid angular intervals, as has been previously discussed [16]. The centers of the angular bins were determined in the following way:

$$\begin{aligned} N_{\mathrm{AZIMUTHAL}} &= \mathrm{round}\left((N_{\mathrm{POLAR}}+1)\sin\theta\right), \\ \phi_k &= -\frac{\pi}{2}+\frac{\pi}{N_{\mathrm{AZIMUTHAL}}}\left(k-\frac{1}{2}\right), \quad k=1,\ldots,N_{\mathrm{AZIMUTHAL}}, \\ \theta_k &= -\frac{\pi}{2}+\frac{\pi}{N_{\mathrm{POLAR}}}\left(k-\frac{1}{2}\right), \quad k-1,\ldots,N_{\mathrm{POLAR}}. \end{aligned} \tag{7}$$

With $N_{\mathrm{POLAR}} = 12$, Eq. (7) produced 100 locations uniformly populating the unit hemisphere.

Three sweep methods were defined from different combinations of the equations and parameters in the above section. In those equations, we used $\Delta L = 30$ mm, $\Delta L' = 25$ mm, and $\Delta B = 0.10$ mT. The "conventional" spectral-spatial imaging used the spectral angles α and the sweep width defined by Eq. (1) and Eq. (3). The spatial and spectral FOV were 30 mm and 0.10 mT (Fig. 1a). The "zoomed-in" imaging (Fig. 1c) used the definitions of Eq. (3) and Eq. (5). The "reduced-sweep" imaging (Fig. 1d) used the definitions of Eq. (1) and Eq. (6). Both the conventional method and the reduced-sweep method required maximum gradient of 30 mT/m. The zoomed-in imaging required maximum gradient of 36 mT/m. Data acquisition time was 55 minutes for the reduced-sweep imaging, and was 68 minutes for each of the other two.

The low SNR at higher gradient projections was partially compensated by signal averaging using the number of averaged projections $N = [(\cos\alpha)^{-1}]$ where the brackets here indicated rounding to the nearest integer less than or equal to the bracketed expression. Each sweep was acquired with 256 field points, 3 ms between analog to digital converter latching of the spectral voltage per point, a 3 ms lock-in amplifier time constant, and with a 12-dB/octave lock-in filter. An SR830 lock-in amplifier (Stanford Research Systems, Sunnyvale, CA) was used. Post processing of the data subjected the projections to a Gaussian filter whose width was 3.2 points. The projections were then subsampled to 256/3.2 = 80 points so that the 4-dimensional image could be reconstructed on a late model PC in a reasonable time (< 2 min).

For a fast reconstruction, we employed multistage FBP that carried out 3 stages of 2D back projections [17]. This required gradient direction sampling aligned in a grid defined by azimuthal and polar angles. We used 2D cubic B-spline interpolation to produce the 12 polar

and 13 azimuthal linear angle sinogram for multistage reconstruction from the 100 projections sampled at uniform solid angles [18]. We then interpolated the 12×13 sinogram by a factor of 4 in each dimension using the same 2D cubic B-spline method.

Simulation with Experimental Noise

To validate the experimental results, we simulated EPRI by forward projecting a 4D synthetic phantom. We incorporated the variation of SNR due to the signal height decrease for high gradient application and its partial compensation by signal averaging. The power spectrum of Gaussian noise was adjusted to match the experimental noise spectrum obtained as above, and the noise level was changed for each gradient magnitude to account for signal averaging. The simulation of reduced sweep imaging generated projections in the same manner as conventional experimental image acquisition, except that the part of the sinogram outside the sweep width defined by Eq. (6) was zero padded. Zoomed in imaging was easily modeled by correspondingly resampling the phantom. We carried out 10 simulations for each of the conventional spectral-spatial method, reduced-sweep method, and zoomed-in method.

Evaluation of image quality using line width resolution and spatial resolution

For the 4D spectral-spatial EPR images obtained with the above procedure, we measured line-width resolutions and spatial resolutions to characterize the performance of each method. The line-width resolution was computed in the following way. First, spatial voxels of the 4D image with signal height greater than 15% of the maximum were selected. Each of the spatial voxel had the corresponding EPR spectrum, which was fitted using the lineshape simulation algorithm [13,14] to extract the Lorentzian line width. We defined the line width resolution as the standard deviation of the line widths from all of the voxels in the phantom with 2 outer layers eroded.

Spectral amplitude at the center of the magnetic field in the 4D image defined a 3D EPR signal height map. We measured the spatial resolution of this 3D signal height map using an edge spread function. This is the response of the system to an edge source modeled by a 2-dimensional step or Heaviside function [19], and is mathematically equivalent to the indefinite integral of a line spread function [20]. The rise of signal height profile of the phantom image was fitted to an error function, from which full width at half maximum (FWHM) of the line spread function was extracted. The spatial resolution was mainly determined by the intrinsic resolution and the finite voxel size of the reconstructed image. With 80 bins for each dimension, the spatial FOV of 30 mm defined the voxel linear dimension of $30\sqrt{2}/80 = 0.53$ mm, which had a non negligible effect on spatial resolution measurement. To evaluate the intrinsic spatial resolution, we approximated the voxelation as a Gaussian spread function, whose width was linearly proportional to the voxel size. Then, the measured spatial resolution S can be specified as a convolution of the intrinsic spatial resolution S_i and the Gaussian spread function. This leads to the following quadrature addition [16].

$$S^2 = S_i^2 + (kD)^2 \tag{8}$$

where k is a dimensionless constant that characterizes the effect of voxel size D. We measured the spatial resolution of images reconstructed with various numbers of bins from 30 to 150, and fitted them to Eq. (8) to estimate S_i. This intrinsic spatial resolution was used to evaluate each sweep method.

After the spectral and spatial fitting procedures, we obtained a mean line width, a line width resolution, and an estimate of the intrinsic spatial resolution from a 4D EPR image. We took

10 images for each of the conventional spectral-spatial method, reduced-sweep method, and zoomed-in method. This resulted in 10 mean line widths, 10 line width resolutions, and 10 intrinsic spatial resolutions for each method. The results presented in Fig. 3 and Fig. 4 have error bars of ±1.96×(standard error of the mean). When the error bars do not overlap, the difference is statistically significant with $p<0.05$ by an unpaired Student t-test [21].

Results

Fitting 100 spectra of the bottle phantom taken without gradient resulted in the line width of 1.44 ± 0.02 μT, where the uncertainty is the standard error of the mean of the measurements. The phantom was oriented as displayed in Fig. 2. The sampling configuration assigned Z axis to the zero polar angle gradient direction. Main magnetic field was parallel to the Z axis and was perpendicular to the cylindrical axis of the phantom. As is shown in Fig. 2b and 2c, none of the images had spatial truncation problem, although the diminished number of spins in each voxel is evident in the diminished apparent intensity (measuring signal height) of Fig. 2c relative to Fig. 2b [22,23].

Fig. 3 shows the mean line widths and the mean line width resolution of each sweep method. Compared with the line width fitted from the spectra under non-imaging condition, a slight broadening (~0.2 μT) was observed. The overlaps of error bars in Fig. 3a indicate a negligible difference in the mean line width measurements. Fig. 3b shows that the difference of line width resolution between the conventional imaging and the reduced-sweep imaging was statistically insignificant. The zoomed-in imaging resulted in a significantly degraded line width resolution.

We measured the spatial resolution both in X and Z directions to estimate the intrinsic spatial resolution for each direction. Fig. 4 shows the intrinsic spatial resolutions in X and Z directions for the images obtained with various sweep methods. The spatial resolutions in the Z direction (Fig. 4a) were better than those in the other direction (Fig. 4b). This was common to all imaging methods. The spatial resolution of reduced-sweep imaging was comparable to the conventional imaging both in X and Z directions. The zoomed-in method that used higher maximum gradient magnitude resulted in a slightly improved spatial resolution.

Table 1 summarizes the results of simulation and experiment for the mean line width and the mean line width resolution. The spatial resolution is shown in Table 2. In general, both the line width resolution and spatial resolution of simulation were slightly better than those of experiment. The zoomed-in imaging shows a significant degradation of line width resolution and an improved spatial resolution compared with the other two imaging methods as seen in the experimental data. The simulation of reduced sweep imaging resulted in a negligible difference in mean line width, mean line width resolution, and spatial resolutions both in X and Z directions.

Discussion

Mean line widths of the fitted image shown in Fig. 3a had a slight increase (~0.2 μT) compared with those obtained under non-imaging conditions. This line broadening is due both to the computation of FBP and to the angular interpolation employed in the reconstruction [18]. Despite uniform solid angle sampling, there was a spatial resolution asymmetry. We observed consistently better spatial resolutions in the Z direction. This is the polar axis of the sampling grid required for the 3-stage 2D reconstruction. We hypothesize that the asymmetric interpolation to uniform linear angle sampling, necessary to use the multi-stage reconstruction resulted in this small direction-dependent spatial resolution [16].

Fig. 3 and Fig. 4 show negligible differences between the fitted values from the conventional sweep method and those from the reduced-sweep method. The reduction of data acquisition

time from 68 min to 55 min did not degrade either the spatial resolution or the line-width resolution of the image. The zoomed-in images had a statistically significant degradation of the line width resolution (Fig. 3b). As is shown in Fig. 2b and 2c, zoomed-in images have decreased spin concentration within each spatial voxel. This decreases SNR and explains the degraded line width resolution. The use of higher maximum gradient magnitude (36 mT/m) than the other two sweep methods (30 mT/m) resulted in a slight enhancement of the intrinsic spatial resolution for the zoomed-in images (Fig. 4). These results can be characterized as a trade-off relationship between the spatial resolution and the line width resolution.

Simulation results followed the same trends as described above. The improved spatial resolution of zoomed in images was accompanied with a degraded line width resolution. The differences between the reduced sweep images and the conventional images were insignificant. The overall superiority of the simulated images to the experimental images implies that the experimental noise model incorporated into the simulation does not completely explain all distortions from the EPR imager, although the similarity of the experimental and simulation results gives a good level of confidence that the simple assumptions of the simulation capture the characteristics of the EPR imager.

In the present work, we confined the variation of the spatial support for EPRI so that none of the images invokes any truncated projections. If a part of the object that produces EPR signal lies outside the spectral-spatial support, the image reconstructed using FBP will suffer from a confounding signal due to the truncated projections [22,23]. This is not because the projections are deficient in information for the full reconstruction of ROI, but because the truncation creates an artifact in the process of FBP. Recently, an exact algorithm has been developed for image reconstruction from truncated data in cone-beam computed tomography [24,25]. Application of the exact ROI reconstruction algorithm to the reduced-sweep imaging will allow the use of truncated projections to result in a substantially shortened imaging time.

Conclusions

When prior knowledge about the size of an imaged object is available, we can exploit the knowledge to optimize the image acquisition in one of several ways. First, one may choose to use a smaller spatial FOV, producing a zoomed-in image that has an enhanced spatial resolution. However, this requires increased gradient magnitudes, and may well be accompanied with the deteriorated line-width resolution. The reduced-sweep method we have developed provides a general approach to the spectral-spatial EPRI. Without changing either the gradient magnitudes or the spatial FOV, this simple modification of the acquisition prunes away the portions of the projection sweep with no signal, shortening the data acquisition time.

We carried out spectral-spatial EPR imaging using different sweep methods. Image quality was evaluated in terms of the spatial resolution and the line width resolution. The zoomed-in images showed a characteristic trade-off relationship between the spatial resolution and the line width resolution with the variation of spatial FOV. The reduced-sweep imaging achieved 20% reduction in data acquisition time without any degradation in the image quality.

Acknowledgments

This work was supported by NIH grants CA98575 and EB002034. Useful discussions with Drs. Xiaochuan Pan and Charles A. Pelizzari are gratefully acknowledged.

References

1. Sotgiu A, Mader K, Placidi G, Colacicchi S, Ursini CL, Alecci M. pH-sensitive imaging by low-frequency EPR: a model study for biological applications. Phys Med Biol 1998;43:1921–1930. [PubMed: 9703055]
2. Halpern HJ, Chandramouli GV, Barth ED, Yu C, Peric M, Grdina DJ, Teicher BA. Diminished aqueous microviscosity of tumors in murine models measured with in vivo radiofrequency electron paramagnetic resonance. Cancer Res 1999;59:5836–5841. [PubMed: 10582707]
3. Kuppusamy P, Li HQ, Ilangovan G, Cardounel AJ, Zweier JL, Yamada K, Krishna MC, Mitchell JB. Noninvasive imaging of tumor redox status and its modification by tissue glutathione levels. Cancer Res 2002;62:307–312. [PubMed: 11782393]
4. Dreher MR, Elas M, Ichikawa K, Barth ED, Chilkoti A, Rosen GM, Halpern HJ, Dewhirst M. Nitroxide conjugate of a thermally responsive elastin-like polypeptide for noninvasive thermometry. Med Phys 2004;31:2755–2762. [PubMed: 15543780]
5. Matsumoto A, Matsumoto S, Sowers AL, Koscielniak JW, Trigg NJ, Kuppusamy P, Mitchell JB, Subramanian S, Krishna MC, Matsumoto K. Absolute oxygen tension (pO2) in murine fatty and muscle tissue as determined by EPR. Magn Reson Med 2005;54:1530–1535. [PubMed: 16276490]
6. Elas M, Ahn KH, Parasca A, Barth ED, Lee D, Haney CR, Halpern HJ. Electron Paramagnetic Resonance Oxygen Images Correlate Spatially and Quantitatively with Oxylite Oxygen Measurements. Clin Cancer Res 2006;12:4209–4217. [PubMed: 16857793]
7. Lauterbur PC, Levin DN, Marr RB. Theory and Simulation of NMR Spectroscopic Imaging and Field Plotting by Projection Reconstruction Involving an Intrinsic Frequency Dimension. J Magn Reson 1984;59:536–541.
8. Maltempo MM. Differentiation of spectral and spatial components in EPR imaging using 2-D image reconstruction algorithms. J Magn Reson 1986;69:156–161.
9. Bowman MK, Michalski TJ, Peric M, Halpern HJ. Fourier-Transform-EPR and Low-Frequency-EPR Studies of Nitroxides. Pure and Applied Chemistry 1990;62:271–274.
10. Mailer C, Subramanian VS, Pelizzari CA, Halpern HJ. Spin echo spectroscopic electron paramagnetic resonance imaging. Magn Reson Med 2006;55:904–912. [PubMed: 16526015]
11. Maltempo MM, Eaton SS, Eaton GR. Spectral-spatial two-dimensional EPR imaging. J Magn Reson 1987;72:449–455.
12. Williams BB, Pan XC, Halpern HJ. EPR imaging: The relationship between CW spectra acquired from an extended sample subjected to fixed stepped gradients and the Radon transform of the resonance density. J Magn Reson 2005;174:88–96. [PubMed: 15809176]
13. Robinson BH, Mailer C, Reese AW. Linewidth analysis of spin labels in liquids. I. Theory and data analysis. J Magn Reson 1999;138:199–209. [PubMed: 10341123]
14. Mailer C, Robinson BH, Williams BB, Halpern HJ. Spectral fitting: The extraction of crucial information from a spectrum and a spectral image. Magn Reson Med 2003;49:1175–1180. [PubMed: 12768596]
15. Halpern HJ, Bowman MK, Spencer DP, Polen JV, Dowey EM, Massoth RM, Nelson AC, Teicher BA. An imaging radiofrequency electron spin resonance spectrometer with high resolution and sensitivity for in vivo measurements. Rev Sci Instr 1989;60:1040–1050.
16. Ahn KH, Halpern HJ. Spatially Uniform Sampling in 4-D EPR spectral-spatial imaging. J Magn Reson. 2007in press
17. Lai CM, Lauterbur PC. A Gradient Control Device for Complete 3-Dimensional Nuclear Magnetic-Resonance Zeugmatographic Imaging. J Phys E Sci Instrum 1980;13:747–750.
18. Ahn KH, Halpern HJ. Comparison of local and global angular interpolation applied to spectral-spatial EPR image reconstruction. Med Phys. 2007in press
19. Bracewell, RN. The Fourier Transform and Its Applications. Vol. 3. McGraw Hill; Boston: 2000.
20. Barrett, HH.; Swindell, W. Radiological Imaging. Vol. revised edition. Academic Press; New York: 1981.
21. Bevington, PR.; Robinson, DK. Data Reduction and Error Analysis. Vol. 3. McGraw-Hill; Boston: 2003.

22. Lewitt RM. Processing of incomplete measurement data in computed tomography. Med Phys 1979;6:412–417. [PubMed: 492075]

23. Natterer, F. The Mathematics of Computerized Tomography. John Wiley & Sons; Chichester: 1986.

24. Zou Y, Pan X. Exact image reconstruction on PI-lines from minimum data in helical cone-beam CT. Phys Med Biol 2004;49:941–959. [PubMed: 15104318]

25. Pan X, Zou Y, Xia D. Image reconstruction in peripheral and central regions-of-interest and data redundancy. Med Phys 2005;32:673–684. [PubMed: 15839339]

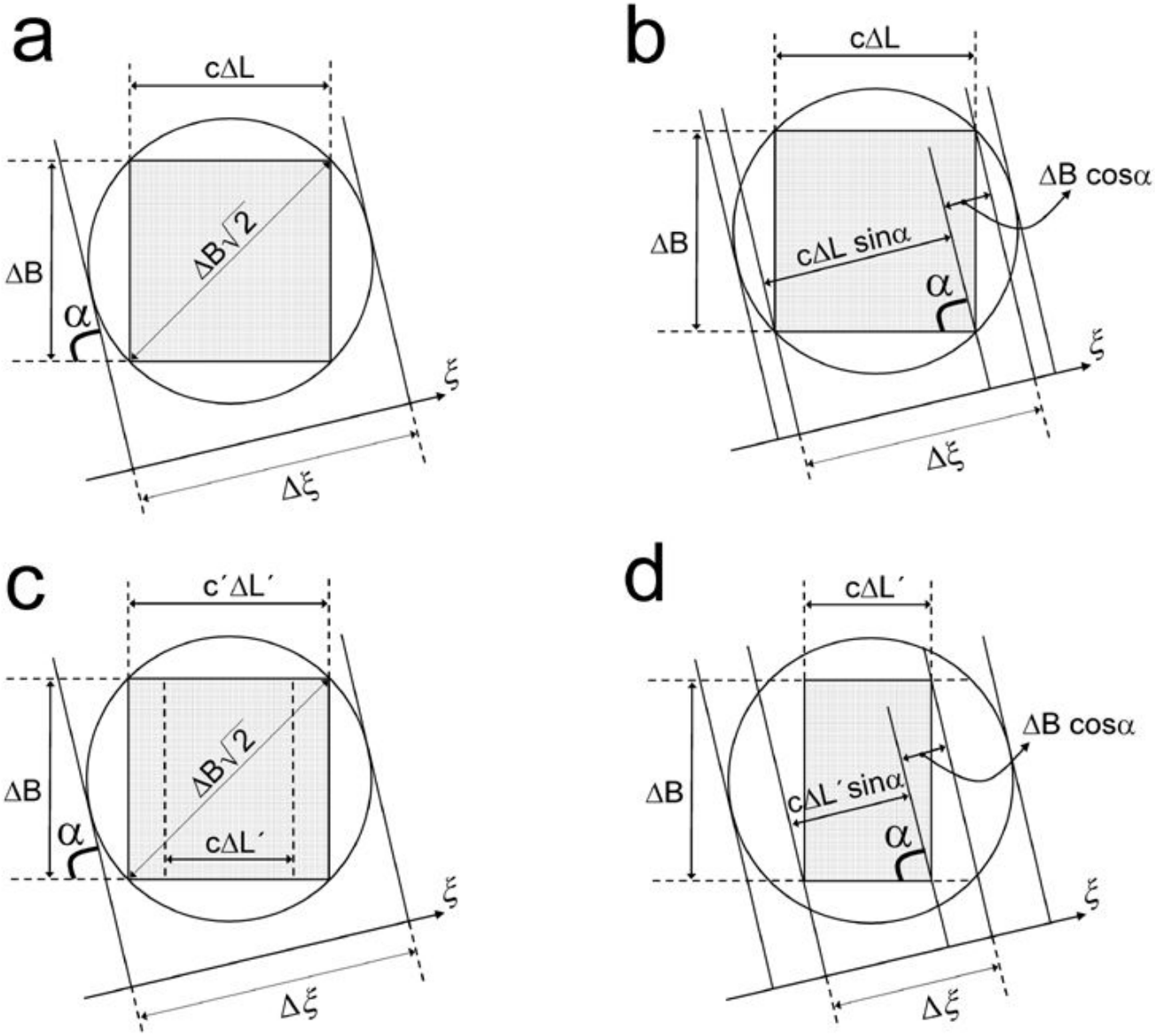

Figure 1.

Definitions of sweep width for spectral-spatial imaging. Shaded rectangles represent the sampled volumes (squeezed hyper-cylinders) of a spectral-spatial object. The 4-D Radon transform derivation of Eq. (2) introduces conversion factors for a unified unit, $c = \Delta B/\Delta L$, and $c' = \Delta B/\Delta L'$. The sweep width ΔB_{SW} is represented by a spectral-spatial variable of $\Delta\xi = \cos\alpha\ \Delta B_{SW}$. (a) Conventional definition of sweep width (Eq. (3)) requires a full sampling in a sphere that encompasses the spectral-spatial object. (b) The definition of Eq. (4) can be explained as an approach to a region of interest (ROI) reconstruction problem. The sampled volume is always covered by field sweeps of varying width. (c) Assignment of the smaller spatial sampling volume to the field of view (FOV) will result in a zoomed-in image. The dashed line inside shaded square demonstrates the zooming effect with the change of conversion factor from c to c'. (d) The sweep width can be further reduced if a spatial extent of object, $\Delta L'$, is known to be smaller than the field of view, ΔL.

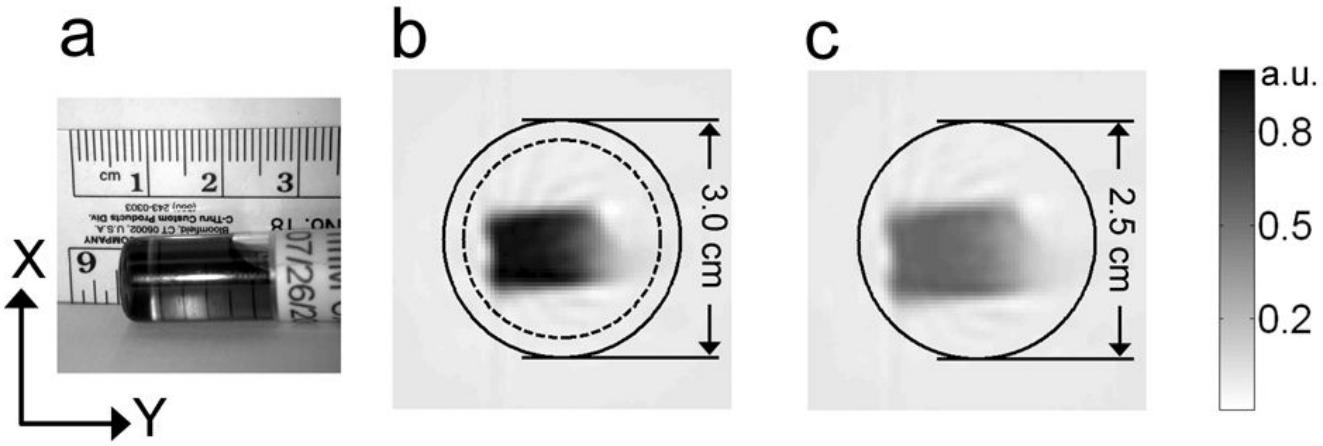

Figure 2.

(a) A sealed borosilicate glass phantom filled with 1 mM deoxygenated OX063 radical. The sampling configuration of the EPR imager assigned Z axis to the zero polar angle gradient direction. The cylindrical Y axis of the phantom was perpendicular to both X and Z axis. (b) XY slice of a 3-D EPR signal height map of the phantom. Solid circle represents the spatial FOV of 3 cm diameter. The inner circle of dashed line has a diameter of 2.5 cm. (c) A zoomed-in image was taken with the spatial FOV of 2.5 cm. The number of spins within each voxel decreased as a result giving a lower signal peak height. The images did not have truncated projections.

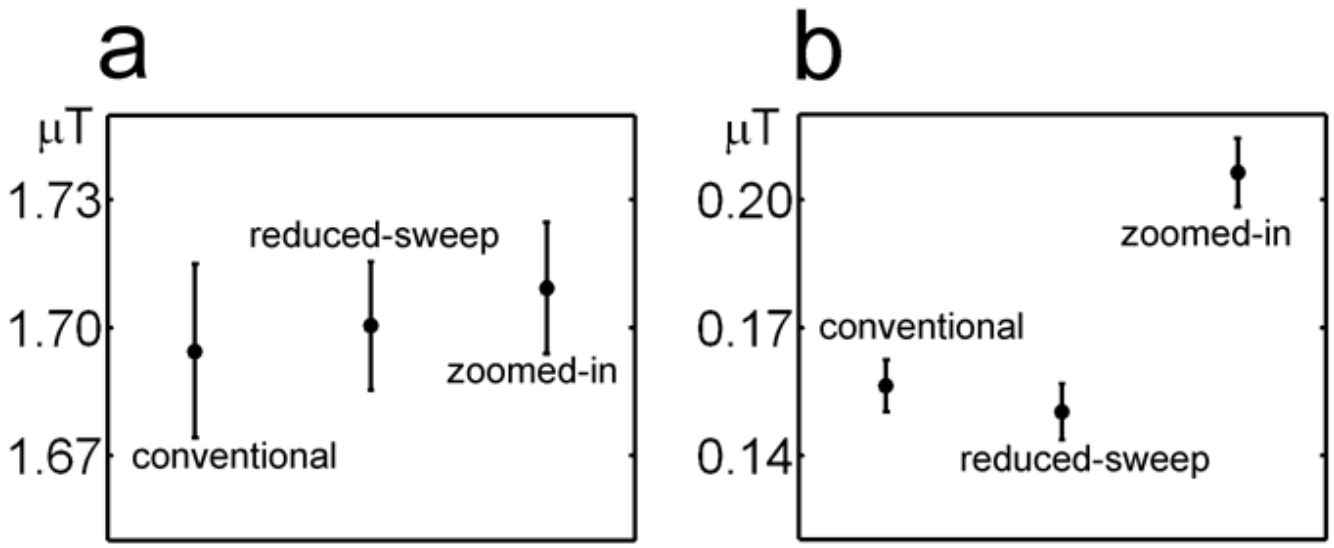

Figure 3.
Spectral parameters fitted from the reconstructed EPR images taken using different sweep methods. Half length of each error bar corresponds to 1.96×(standard error of the mean). (a) Mean line widths. (b) Mean line width resolutions.

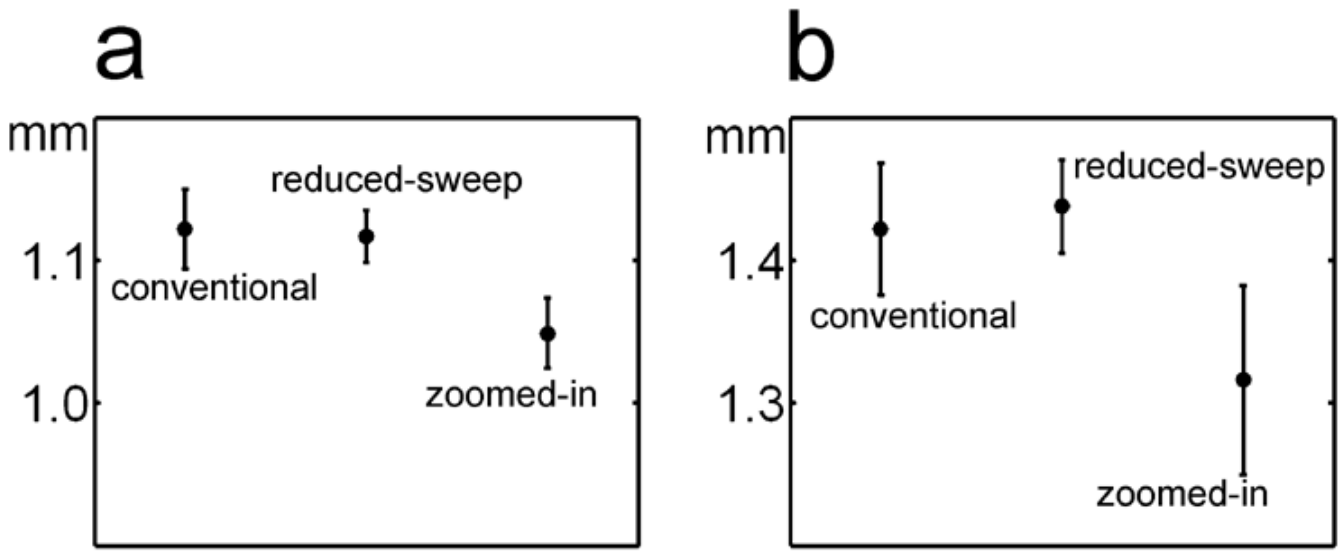

Figure 4.

Intrinsic spatial resolutions (FWHM) of the EPR images taken using different sweep methods. The spatial resolution was measured both in X and Z directions. The coordinate system is described in Figure 2. Half length of each error bar corresponds to 1.96×(standard error of the mean). (a) Spatial resolution measured in Z direction. (b) Spatial resolution measured in X direction.

Table 1

Fitted line widths from EPRI experiment† and simulation‡

	conventional	reduced sweep	zoomed-in
mean line width (experiment) mean line width resolution (experiment)	1.69 ± 0.01 μT 0.161 ± 0.004 μT	1.70 ± 0.01 μT 0.155 ± 0.004 μT	1.71± 0.01 μT 0.21 ± 0.01 μT
mean line width (simulation) mean line width resolution (simulation)	1.69 μT 0.13 μT	1.69 μT 0.13 μT	1.69 μT 0.16 μT

† Average values of 10 repeated experiments ± standard error

‡ Average values of 10 repeated simulations. Standard errors were below 1% of each measurement.

Table 2

Spatial resolution (FWHM) from EPRI experiment[†] and simulation[‡]

	conventional	reduced sweep	zoomed-in
X direction (experiment)	1.42 ± 0.02 mm	1.44 ± 0.02 mm	1.34 ± 0.04 mm
Z direction (experiment)	1.12 ± 0.01 mm	1.12 ± 0.01 mm	1.06 ± 0.01 mm
X direction (simulation)	1.16 mm	1.15 mm	1.01 mm
Z direction (simulation)	1.08 mm	1.08 mm	0.87 mm

[†]Average values of 10 repeated experiments ± standard error

[‡]Average values of 10 repeated simulations. Standard errors were below 1% of each measurement.